

Distribution of Si, Fe, and Ni in the Intracluster Medium of the Coma Cluster

Kyoko MATSUSHITA¹, Takuya SATO¹, Eri SAKUMA¹, and Kosuke SATO¹.

¹ *Department of physics, Tokyo University of Science, 1-3 Kagurazaka, Shinjuku-ku, Tokyo 162-8601*
matusita@rs.kagu.tus.ac.jp

(Received —; accepted —)

Abstract

We studied the distributions of Si, Fe, and Ni in the intracluster medium (ICM) of the Coma cluster, one of the largest clusters in the nearby universe, using XMM-Newton data up to $0.5 r_{180}$ and Suzaku data of the central region up to $0.16 r_{180}$. Using the flux ratios of Ly α line of H-like Si and 7.8 keV line blend to K α line of He-like Fe, the abundance ratios of Si to Fe and Ni to Fe of the ICM were derived using APEC model v2.0.1. The Si/Fe ratio in the ICM of the Coma cluster shows no radial gradient. The emission weighted averages of the Si/Fe ratio in the ICM within $0.0\text{--}0.2 r_{180}$, $0.2\text{--}0.5 r_{180}$, and $0.0\text{--}0.5 r_{180}$ are 0.97 ± 0.11 , 1.05 ± 0.36 and 0.99 ± 0.13 , respectively, in solar units using the solar abundance table by Lodders (2003). These values are close to those of smaller clusters and groups of galaxies. Using the Suzaku data of the central region, the derived Ni/Fe ratio of the ICM is 0.6–1.5 in solar units, according to the same solar abundance table. The systematic difference in the derived abundance ratios by different plasma codes are about 10%. Therefore, for the ICM in the Coma cluster, the abundance pattern of Si, Fe, and Ni is consistent with the same mixture of the yields of supernova (SN) II and SN Ia in our Galaxy. Within $0.5 r_{180}$, the cumulative iron-mass-to-light ratio increases with radius, and its radial profile is similar to those of relaxed smaller clusters with cD galaxies at their center. Using the observed Si/Fe ratio, the cumulative metal-mass-to-light ratios at $0.5 r_{180}$ are compared with theoretical expectations.

Key words: galaxies:clusters:individual (Abell 1656, the Coma cluster) — X-rays:galaxies — X-rays:intracluster medium

1. Introduction

An important clue to the evolution of galaxies is the metals in the intracluster medium (ICM). Because the Fe–K lines are prominent in the spectra of the ICM, the Fe abundance in the ICM has been studied in detail. With ASCA observations, Fukazawa et al. (2000) found that clusters with a sharp X-ray emission centered on a cD galaxy commonly exhibit a central increment in the Fe abundance of the ICM. With Beppo-SAX observations, de Grandi & Molendi (2001) also found a difference in the Fe abundance profiles between clusters with and without cool-cores. With XMM-Newton observations, Johnson et al. (2011) found a similar trend among groups of galaxies. Within cool cores of clusters and groups of galaxies, the central Fe peak could have been mainly produced by type Ia supernovae (SNe) in cD galaxies. In contrast, during cluster merging, mixing of the ICM could destroy the cool cores and the central Fe peaks.

Since metals have been synthesized by SNe in galaxies, the ratios of metal mass in the ICM to the total light from galaxies in clusters or groups, i.e., the metal-mass-to-light ratios, are the key parameters in investigating the chemical evolution of the ICM. With ASCA observations, the derived ratios of Fe mass in the ICM to the total light from galaxies, iron-mass-to-light ratio (IMLR), within a radius where the ICM density falls below $3 \times 10^{-4} \text{ cm}^{-3}$ is nearly constant in rich clusters and

decreases toward poorer systems (Makishima et al. 2001). In individual clusters, the IMLR is lower around the center (Makishima et al. 2001). With Chandra, XMM, and Suzaku observations of groups and medium-size clusters, the lower IMLR within a given over-density radius in some groups of galaxies have been confirmed (Matsushita et al. 2007a; Tokoi et al. 2008; Rasmussen & Ponman 2009; Sato et al. 2009a; Sato et al. 2009b; Sato et al. 2010; Komiyama et al. 2009; Sakuma et al. 2011; Murakami et al. 2011).

Since Fe is both synthesized in SN Ia and SN II, to constrain contributions from the two types of SN, we need measurements of abundances of various elements. The ASCA satellite first studied the Si abundance in the ICM (Fukazawa et al. 1998; Fukazawa et al. 2000; Finoguenov et al. 2000; Finoguenov et al. 2001). Fukazawa et al. (1998) reported that the Si/Fe ratio in the ICM increases with ICM temperature, suggesting that the relative contribution of SN II increasing towards massive clusters. Finoguenov et al. (2000) reported that the Si/Fe ratio increases with radius in several clusters. Using Chandra data of groups out to r_{500} , Rasmussen & Ponman (2007) found that SN II contribution increases with radius and completely dominates at r_{500} . XMM-Newton and Suzaku observations also have been used to study the Si/Fe ratio of the ICM in clusters and groups of galaxies. (Matsushita et al. 2003; Tamura et al. 2004; Sanders & Fabian 2006; Werner et al. 2006; de Plaa et al. 2007; Rasmussen & Ponman 2007; Matsushita et al. 2007a; Matsushita et

al. 2007b; Sato et al. 2007a; Sato et al. 2007b; Sato et al. 2008; Tokoi et al. 2008; Komiyama et al. 2009; de Grandi & Molendi 2009; Simionescu et al. 2009; Sato et al. 2009a; Sato et al. 2009b; Sato et al. 2010; Sakuma et al. 2011; Murakami et al. 2011). With Suzaku observations of clusters and groups with the ICM temperatures lower than ~ 4 keV, the derived values of Si abundance are close to those of Fe (the Si/Fe ratios are ~ 0.8 in solar units) out to $0.2\text{--}0.3 r_{180}$, with a small scatter using the solar abundance table by Lodders (2003). In the core regions, the reported values of the Si/Fe ratios have a larger scatter (de Plaa et al. 2007; de Grandi & Molendi 2009). With XMM-Newton observations of nearby clusters, Tamura et al. (2004) found that the temperature dependence does not exist in the Si/Fe ratios. For example, the Si/Fe ratio outside the cool core of the Perseus cluster is 0.77 ± 0.25 in solar units using the same solar abundance table. However, excluding cool core regions, the error bars in the Si/Fe ratio of hotter clusters are very large.

With Beppo-SAX observations, de Grandi & Molendi (2002) reported that cooling flow clusters show higher Ni abundances in their cores than non-cooling flow clusters. Baumgartner et al. (2005) analyzed hundreds of clusters observed with ASCA and reported that the average Ni abundance in hot clusters is about 1.3 solar, which is significantly higher than the Fe abundances in the ICM. In the cool core of the Perseus cluster, the Ni/Fe ratio is consistent with the solar ratio (Churazov et al. 2004; Tamura et al. 2009; Matsushita & Tamura 2011), whereas that of the Centaurus cluster is significantly higher (Matsushita & Tamura 2011). de Plaa et al. (2007) found that the weighted average of the Ni/Fe ratios of core regions of nearby clusters was 1.4 ± 0.3 with respect to solar ratio by Lodders (2003). de Grandi & Molendi (2009) studied Si, Fe, and Ni abundances in the central regions of 26 local clusters and discovered that the Ni/Fe ratio scatters significantly. In our Galaxy, [Ni/Fe] of stars are ~ 0 , with no dependence of [Fe/H] (Edvardsson et al. 1993; Feltzing & Gustafsson 1998; Gratton et al. 2003). This result indicates that in our Galaxy both SN II and SN Ia synthesize Ni in a similar manner as that of Fe. In cool cores, the enhancement of Fe abundance indicate the metal production from cD galaxies (e.g. Böhringer et al. 2004). Therefore, the higher Ni/Fe ratios observed in some clusters indicate that Ni synthesis in cD galaxies differ from that in our Galaxy. However, in some cases, Ni abundances are derived from the spectral fitting including the Fe-L energy band. Then, Ni abundance is derived from residuals between data and the Fe-L model, which strongly depends on the plasma codes. With CCD detectors, the $K\alpha$ lines of He-like Ni and $K\beta$ lines of He-like Fe are blended into a single bump at 7.8 keV, and the derived Ni abundance couples with the effect of resonant line scattering (Churazov et al. 2004; Matsushita & Tamura 2011). Therefore, for cases in which the optical depth for the scattering is sufficiently small, spectral fittings of K lines of Ni give more reliable Ni abundances.

The Coma cluster ($z = 0.0231$), also known as Abell 1656, is one of the largest clusters in the nearby

universe. The cluster does not have a strong cool-core in the center, and the X-ray peak is not associated with two dominant galaxies in the central region (Vikhlinin et al. 1994). With Chandra observations, Vikhlinin et al. (2001) found that these dominant galaxies retain their X-ray corona in the form of compact halo (a few kpc in size) with temperatures of 1–2 keV. Using XMM-Newton data, Arnaud et al. (2001) found a temperature drop within 1 arcmin from one of the dominant galaxies, NGC 4874. However, they reported that the projected temperature distribution of most of the core region is remarkably homogeneous. Using Suzaku data, Sato et al. (2011) reported that fittings of the continuum spectra and the ratio of the $Ly\alpha$ line of H-like Fe and $K\alpha$ line of He-like Fe implied the same ICM temperatures. Because line ratio is a steep function of temperature, this consistency supports the accuracy of temperature measurements using Suzaku. Matsushita (2011) and Sato et al. (2011) derived the Fe abundance profile in the ICM up to $\sim 0.5 r_{180}$. Within $0.2 r_{180}$, the Fe abundance is flat at ~ 0.4 solar, according to the solar abundance table by Lodders (2003), and further decreases with radius. This flat Fe abundance is significantly different from the peaked abundance profiles of cool-core clusters and indicates that the gases have been mixed well in the core during the past mergers associated with cluster growth.

In this paper, we study Si/Fe and Ni/Fe ratios in the ICM of the Coma cluster observed with XMM and Suzaku. In addition, we derived IMLR profiles of the Coma cluster and compared the results with smaller clusters. The paper is organized as follows; After the introduction, we present the observations in section 2, followed by the description of our data analysis and results in section 3. In section 4, we discuss our results.

We used the Hubble constant, $H_0 = 70 \text{ km s}^{-1} \text{ Mpc}^{-1}$. The distance to the Coma cluster is $D_L = 101 \text{ Mpc}$, and $1'$ corresponds to 28 kpc. The virial radius of the Coma cluster, $r_{180} = 1.95 h_{100}^{-1} \sqrt{k\langle T \rangle} / 10 \text{ keV Mpc}$ (Evrard et al. 1996; Markevitch et al. 1998), is 2.5 Mpc for the average temperature $k\langle T \rangle = 7.8 \text{ keV}$. We used the solar abundance ratio by Lodders (2003), in which the solar Si, Ni and Fe abundances relative to H are 3.47×10^{-5} , 1.66×10^{-6} , and 2.95×10^{-5} , respectively, by number. Considering a difference in solar He abundance, the Fe abundance yielded by Lodders (2003) is 1.5 times higher than that using the photospheric value by Anders & Grevesse (1989). Using the table by Lodders (2003), the Si/Fe and Ni/Fe ratios are factors of 1.55 and 1.48, respectively, smaller than those from Anders & Grevesse (1989). Errors are quoted at 90% confidence level for a single parameter. The spectral analysis employed the XSPEC_v12.7.0 package.

2. Observation and Data Reduction

2.1. XMM observations

We analyzed 25 pointings of XMM-Newton observations of the Coma cluster using PN, MOS1, and MOS2 detectors. In this study, we used SASv10.0, but the details of observations, event selection, and background subtraction

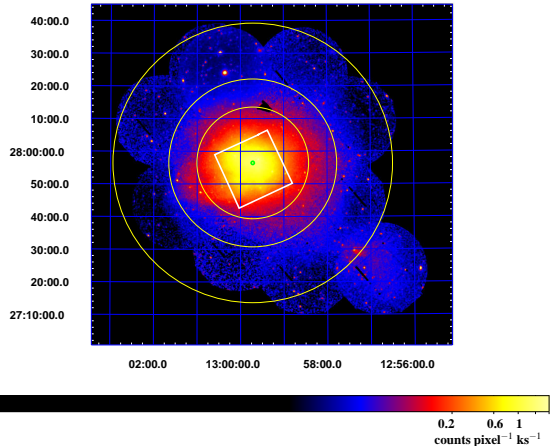


Fig. 1. Exposure-corrected combined MOS image of the Coma cluster (0.5–4.0 keV). The green circle corresponds to the X-ray peak, and the white square indicates the field of view (FOV) of the Suzaku. Yellow circles have radii of 0.2, 0.3, and 0.5 r_{180} .

are the same as those in Matsushita (2011). The exposure corrected combined MOS image of the Coma cluster within an energy range of 0.5–4.0 keV is shown in Figure 1. Spectra were accumulated over annular regions centered on the X-ray peak of the cluster. The spectra from MOS1 and MOS2 were added.

2.2. *Suzaku* observation

We analyzed *Suzaku* XIS (Koyama et al. 2007) data of the central region of the Coma cluster, whose *Suzaku* sequence number is 801097010, observed in 2006 May with an exposure of 150 ks. The XIS instrument consists of four X-ray CCD (XIS0, 1, 2, and 3). XIS1 is a back-illuminated (BI) sensor, while XIS0, 2, and 3 are front-illuminated (FI) ones. Figure 1 shows the field of view (FOV) of the XIS. We used *HEASoft* version 6.11, and *CALDB* 2011-02-10, but the details of observations, data reduction, background subtractions and response matrix are the same as those in Sato et al. (2011). We extracted spectra over the FOV of the XIS, except for the regions around calibration sources.

3. Analysis and Results

3.1. Radial profile of *Si/Fe* ratio

With the CCD response and a typical Si abundance, the peak level of the $\text{Ly}\alpha$ line of H-like Si of a 8 keV plasma in a spectrum is only a few percent above that of the continuum and a small systematic uncertainty in the response matrix can cause a large systematic uncertainty in the Si abundance. We first fitted the MOS and PN spectra at 0.06–0.2 r_{180} with a single-temperature *vAPEC* model v2.0.1 (Smith et al. 2001). Using an energy range of 0.5–7.2 keV, the two kind of detectors gave temperatures and Si abundances of 8.2–8.3 keV and 0.0 solar, respectively, and there are discrepancies of a few percent between the data and model around the $\text{Ly}\alpha$ line of H-like Si. Next,

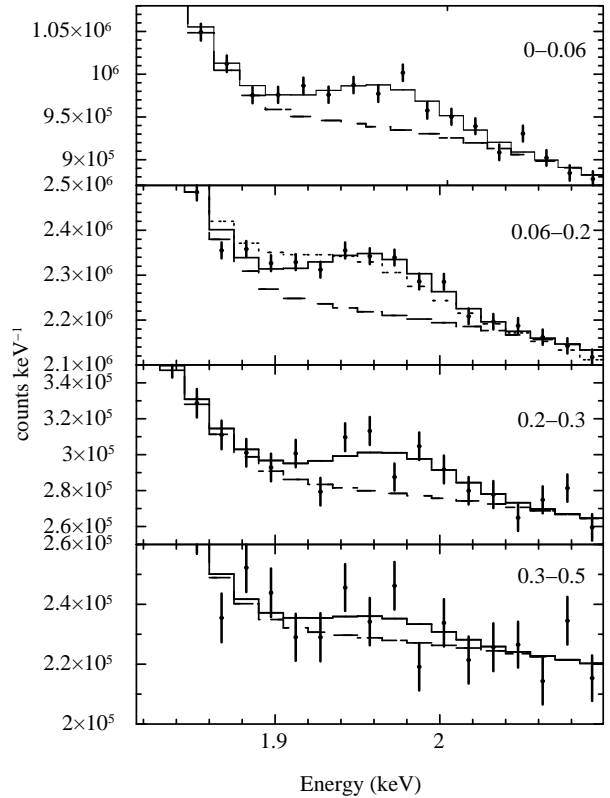


Fig. 2. MOS spectra at 0.0–0.06, 0.06–0.2, 0.2–0.3, and 0.3–0.5 r_{180} (from top to bottom) fitted with an *vAPEC* v2.0.1 model with Si abundance = 0 solar (dashed line) and a Gaussian. The dotted line at 0.06–0.2 r_{180} corresponds to the best-fit single-temperature APEC model fitted within an energy range of 1.8–2.1 keV, where the best-fit Si abundance was 0.1 solar.

we restricted the energy range to 1.8–2.1 keV, and refitted the spectra. Then, the best-fit Si abundance derived from MOS and PN were 0.1 and 0.5 solar, respectively. In this case, reduced χ^2 for the MOS spectrum was still greater than 2, and the discrepancies between the data and model were around a few percent at maximum (see Figure 2). In contrast, χ^2 for the PN spectrum became acceptable. Furthermore, the best-fit ICM temperatures, 5.4 keV and 11.7 keV, respectively, differed significantly from those derived from the wider energy range. Using the older version of response matrices by SAS-8.0 also gave significantly different Si abundances. These results indicate a minor difference in the response files around the Si line caused a significant discrepancy in the derived Si abundance. For the *Suzaku* XIS detectors, severe discrepancies at 1.7–1.9 keV and 2.1–2.2 keV between the *Suzaku* FI and BI responses were reported (Sato et al. 2011).

We added a 1% systematic error to the counts of each channel in the spectra of MOS and PN, and simultaneously fitted MOS and PN spectra within energy ranges of 1.8–2.1 keV and 1.8–2.2 keV, respectively, with a single-temperature *vAPEC* v2.0.1 model. We also fitted the XIS FI and BI spectra simultaneously within an energy range of 1.92–2.1 keV in the same way. Here, the Si abundance was allowed to vary and those of the other metals were

Table 1. Results of spectra fits around the Ly α -line of H-like Si with a vAPEC v2.0.1 model.

radius (r_{180})	detector	Si/Fe (solar ratio)	$\chi^2/d.o.f$
0.0–0.06	MOS, PN	1.00 ± 0.23	28/35
0.06–0.2	MOS, PN	0.89 ± 0.21	34/35
0.2–0.3	MOS, PN	1.23 ± 0.49	36/35
0.3–0.5	MOS, PN	0.79 ± 0.53	39/35
0.0–0.16	XIS0123	0.70 ± 0.20	14/19

fixed to the best-fit Fe abundance derived in Matsushita (2011). Temperature was fixed to the best-fit value derived in Matsushita (2011), since the equivalent width of the Si line at fixed Si abundance depends on the plasma temperature. Above 1.8 keV, a systematic uncertainty caused by strong instrumental fluorescence line at ~ 1.7 keV of the MOS detector does not affect the derived Si abundance. Table 1 shows χ^2 and the derived Si/Fe ratios using the Fe abundances derived in Matsushita (2011). The χ^2 became acceptable. As shown in the left panel in Figure 3, the derived Si/Fe ratios are consistent with the solar ratio and show no radial gradient. The XIS spectra within $0.16 r_{180}$ gave a smaller Si/Fe ratio of 0.7 ± 0.2 , in units of the solar ratio. The emission weighted averages of the Si/Fe ratio with MOS and PN within $0.0\text{--}0.2 r_{180}$, $0.2\text{--}0.5 r_{180}$, $0.0\text{--}0.5 r_{180}$ are 0.94 ± 0.16 , 1.09 ± 0.37 and 0.98 ± 0.16 , respectively, in units of the solar ratio.

With the APEC model v2.0.1, the ratio of Ly α line of H-like Si and K α line of He-like Fe is, at fixed Si/Fe ratio, constant to within 10% across the $kT=6\text{--}12$ keV temperature range (the right panel of Figure 3). The weak temperature dependence of the line ratio can minimize the effect of uncertainties in the temperature structure of the ICM. Therefore, we also derived the line flux of these two lines and converted their ratios to abundance ratios of Si to Fe using the theoretical expectations. To derive line strengths of the Ly α of H-like Si, we fitted spectra of MOS, PN, and XIS-BI and XIS-FI detectors within an energy range of 1.8–2.1 keV, 1.8–2.2 keV, 1.92–2.1 keV, and 1.92–2.1 keV, respectively, with a sum of vAPEC model and a Gaussian for the Ly α line of H-like Si. Considering differences in energy resolution, we used a wider energy range for PN. Here, we used spectra without systematic error to the counts of each channel. The Si abundance of the vAPEC model was fixed at 0, and the abundances of the other metals were fixed to the best-fit Fe abundance derived in Matsushita (2011). Because of the high ICM temperature of the Coma cluster, the K α line of He-like Si is negligible. To derive line strengths of Fe, we also fitted these spectra within an energy range of 6.0–7.2 keV with a bremsstrahlung and two Gaussians for He-like and H-like Fe lines.

Table 2 summarizes the results of the line ratio. The values of χ^2 are reasonable. As shown in Figure 2, the Ly α line of the H-like Si is clearly seen in the spectra, and well reproduced with the model. The MOS, PN, and XIS detectors gave almost the same line ratios of the Ly α

Table 2. Line ratio of the Ly α of H-like Si and K α of He-like Fe and the Si/Fe ratio

radius (r_{180})	detector	$F_{\text{Si}}/F_{\text{Fe}}$ *	Si/Fe \dagger (solar ratio)	$\chi^2/d.o.f$ \ddagger
0.0–0.06	MOS	$0.29^{+0.08}_{-0.08}$	$1.00^{+0.28}_{-0.28}$	18.1/15
0.06–0.2	MOS	$0.30^{+0.06}_{-0.09}$	$1.03^{+0.22}_{-0.31}$	15.1/15
0.2–0.3	MOS	$0.39^{+0.16}_{-0.15}$	$1.30^{+0.58}_{-0.56}$	20.4/15
0.3–0.5	MOS	$0.14^{+0.17}_{-0.14}$	$0.39^{+0.55}_{-0.39}$	18.8/15
0.0–0.06	PN	$0.35^{+0.07}_{-0.09}$	$1.20^{+0.24}_{-0.32}$	13.7/11
0.06–0.2	PN	$0.24^{+0.07}_{-0.07}$	$0.82^{+0.25}_{-0.24}$	7.0/11
0.2–0.3	PN	$0.40^{+0.23}_{-0.24}$	$1.33^{+0.82}_{-0.84}$	8.6/11
0.3–0.5	PN	$0.47^{+0.43}_{-0.47}$	$1.30^{+1.42}_{-1.30}$	9.2/11
0.0–0.16	XIS1	$0.25^{+0.06}_{-0.10}$	$0.86^{+0.21}_{-0.35}$	4.5/7
0.0–0.16	XIS023	$0.33^{+0.07}_{-0.08}$	$1.14^{+0.24}_{-0.28}$	8.8/7

* Ratio of flux in units of photons $\text{cm}^{-2}\text{s}^{-1}$ of Ly α line of H-like Si and K α line of He-like Fe.

\dagger Si/Fe abundance ratio in units of solar ratio derived from the line ratio using the theoretical expectation from APEC v2.0.1.

\ddagger χ^2 and degrees of freedom of the spectral fitting around the Ly α line of H-like Si.

of H-like Si to the K α line of He-like Fe (Table 2 and the right panel of Figure 3). The derived line ratios are consistent with the theoretical expectations by the APEC v2.0.1, v1.3 and MEKAL(Mewe et al. 1985; Mewe et al. 1986; Kaastra 1992; Liedahl et al. 1995) codes with a solar Si/Fe ratio. Using APEC v2.0.1 code, we converted the derived line ratios to the abundance ratio of Si/Fe using the temperatures derived by Matsushita (2011), since Sato et al. (2011) found that the single-temperature model fits the Suzaku spectra of the Coma cluster fairly well. Here, we allowed a 10% systematic error in the temperature for the XMM data (see details in Matsushita 2011). The systematic effect by the plasma code on the Si/Fe ratio is expected to be insignificant because the MEKAL and APEC v2.0.1 codes gave similar line ratios within 10% at 8 keV and APEC v1.3 and APEC v2.0.1 gave almost the same line ratio (Figure 3). Therefore, the systematic difference in the derived Si/Fe ratio by different plasma codes is about 10%, which is smaller than the statistical errors.

The left panel of Figure 3 also shows the radial profile of the Si/Fe ratio derived from the line ratio. The derived abundance ratios from MOS and PN agree very well with those derived from spectral fitting with APEC model around the Ly α line of H-like Si. Using MOS, PN and XIS detectors, the emission weighted average of the Si/Fe abundance ratio from the line ratio within $0.0\text{--}0.2 r_{180}$, $0.2\text{--}0.5 r_{180}$, and $0.0\text{--}0.5 r_{180}$ are 0.97 ± 0.11 , 1.05 ± 0.36 , and 0.99 ± 0.13 , respectively, in units of the solar ratio. These values are consistent with those derived from the spectral fitting around the Si lines within 10%.

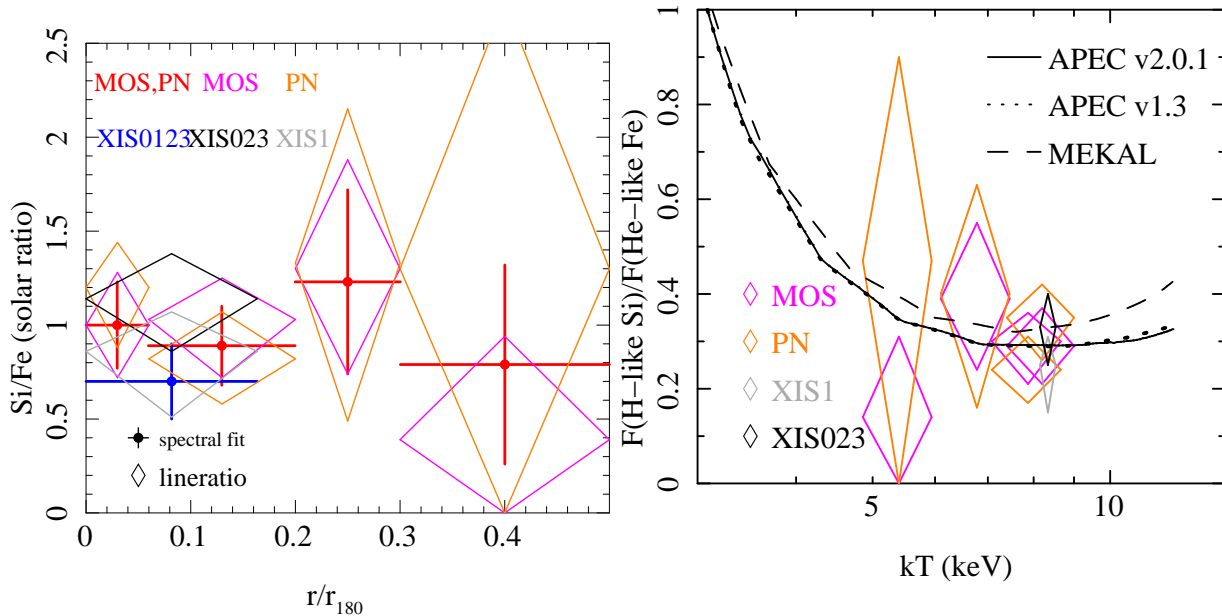


Fig. 3. (left panel) The radial profiles of the Si/Fe ratio in solar units derived from spectral fitting with vAPEC model v2.0.1 around the Si line (closed circles with error bars) using MOS and PN (red) and XIS detectors (blue). Those derived from the line ratio of Ly α of H-like Si to K α of He-like Fe (diamonds) using MOS (magenta), PN (orange), XIS-FI (black), and XIS-BI (gray) are also plotted. Here, we used vAPEC v2.0.1 model. (right panel) Flux ratios of Ly α line of H-like Si to K α line of He-like Fe derived from MOS (magenta), PN (orange), Suzaku XIS-FI (black) and XIS-BI (gray) plotted against plasma temperature derived by Matsushita (2011) and Sato et al. (2011). The temperatures and line ratios were derived within the radial range listed in Table 2. We added a 10% systematic uncertainty in plasma temperature derived with XMM-Newton data (Matsushita 2011). The solid, dotted, and dashed lines indicate theoretical ratios with a plasma of solar Si/Fe ratio according to APEC v2.0.1, APEC v1.3, and MEKAL plasma codes, respectively.

3.2. Ni/Fe ratio of the central region

To derive Ni abundance, we used only Suzaku spectra of the central field (0–0.16 r_{180}) because of its lower level of background. We added the spectra of the FI detectors, XIS0, XIS2, and XIS3. We fitted background-subtracted Suzaku spectra of the FI and BI detectors simultaneously within an energy range of 3.0–8.5 keV with a vAPEC plasma model v2.0.1. Here, elemental abundances except for Fe and Ni were fixed at 0.4 solar, since Fe abundance of this region derived with Suzaku (Sato et al. 2011) and XMM (Matsushita 2011) is nearly constant at this value. The derived ICM temperature, the Fe and Ni abundances are 8.4 ± 0.05 keV, 0.39 ± 0.01 solar, and 0.66 ± 0.10 solar, respectively. The derived ICM temperature and Fe abundance are consistent with those derived by Sato et al. (2011) and Matsushita (2011). However, the derived χ^2 , 719 for 560 degrees of freedom, was not acceptable, considering only statistical errors. Therefore, we restricted energy range to 7.1–8.4 keV and fitted the spectra again with a vAPEC plasma model v2.0.1. Here, the temperature and Fe abundance were fixed at 8.4 keV and 0.39 solar, respectively. The results are shown in Figure 4 and Table 3. The spectra were better fitted with the model, with $\chi^2=142$ for 128 degrees of freedom. The derived Ni abundance, 0.48 ± 0.13 solar, became smaller than the previous fit using the wider energy range. When we used the energy range to 7.3–8.4 keV, the Ni abundance became 0.43 ± 0.14 solar, with a better reduced χ^2 (Table 3). We

Table 3. Results of spectral fitting of the Suzaku central field*.

model	energy range (keV)	Ni (solar)	$\chi^2/d.o.f$
vAPEC v2.0.1	7.1–8.4	0.48 ± 0.13	142/128
vAPEC v2.0.1	7.3–8.4	0.43 ± 0.14	109/109
vAPEC v1.3	7.1–8.4	0.50 ± 0.13	146/128
vMEKAL	7.1–8.4	0.51 ± 0.12	167/128

* The temperature and the Fe abundances were fixed at 8.4 keV and 0.39 solar, respectively.

also fitted the same spectra using the energy range of 7.1–8.4 keV in the same way with vAPEC v1.3 and vMEKAL plasma codes. As shown in Table 3, the vAPEC v1.3 code gave almost the same results with the vAPEC v2.0.1 code. The vMEKAL code also gave almost the same Ni abundance, although the fit with the vMEKAL model around 8.2–8.3 keV, at the line blend of K γ line of He-like Fe and K β line of H-like Fe, is significantly worse than those using vAPEC models (Figure 4).

As in section 3.1 for the Si/Fe ratio, we derived the flux ratio of the 7.8 keV line blend to K α line of He-like Fe line and converted it to the Ni/Fe ratio. We fitted the same Suzaku spectra of XIS-FI and XIS-BI within the energy range of 7.1–8.4 keV with a bremsstrahlung and two Gaussians for the line blends of the 7.8 keV and 8.3

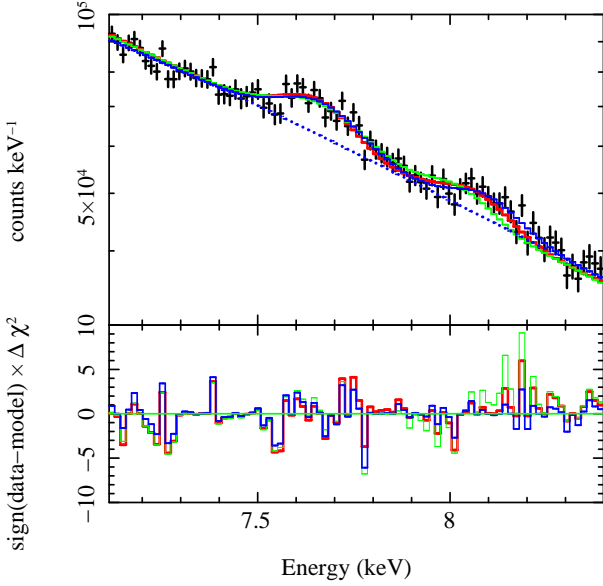


Fig. 4. The spectrum of the XIS-FI of the central field of Suzaku fitted with a vAPEC v2.0.1 model (red), vMEKAL model (green) and bremsstrahlung and Gaussians (blue) within an energy range of 7.1–8.4 keV. The blue dotted line corresponds to the contribution of the continuum of the Gaussian fit. The bottom panel shows the contributions to the χ^2 .

Table 4. Results of spectral fits with a bremsstrahlung and Gaussians using an energy range of 7.1–8.4 keV.

Gaussian center * (keV)	F(line)/F(6.7) †
7.84 ± 0.02	0.166 ± 0.026
8.27 ± 0.02	0.090 ± 0.021
$\chi^2/d.o.f$	127/121

* The central energy at the rest-frame of the Coma cluster

† Ratio of flux in units of photons $\text{cm}^{-2}\text{s}^{-1}$ of the 7.8 keV or 8.3 keV blends to $K\alpha$ line of He-like Fe.

keV. The line widths of the Gaussians are fixed to those derived from fitting of a mock XIS spectrum of 8.3 keV plasma with vAPEC v.2.0.1.

The results are shown in Table 4. The spectra were well represented with the model with $\chi^2 = 127$ for 121 degrees of freedom (Table 4 and Figure 4). Figure 5 shows the ratio of the flux of the 7.8 keV blend to that of the $K\alpha$ line of He-like Fe, plotted against the plasma temperature. The theoretical temperature dependence of the ratio and the discrepancy between the three codes are relatively small. The derived ratio, 0.166 ± 0.026 , agrees with the expectation of the APEC models with the solar Ni/Fe ratio. Converting the derived ratio to the abundance ratio, the Ni/Fe ratio became 0.6–1.5, and 0.9–1.6, in units of solar ratio, using the APEC codes and MEKAL code, respectively.

The worse χ^2 with the MEKAL model reflects the dis-

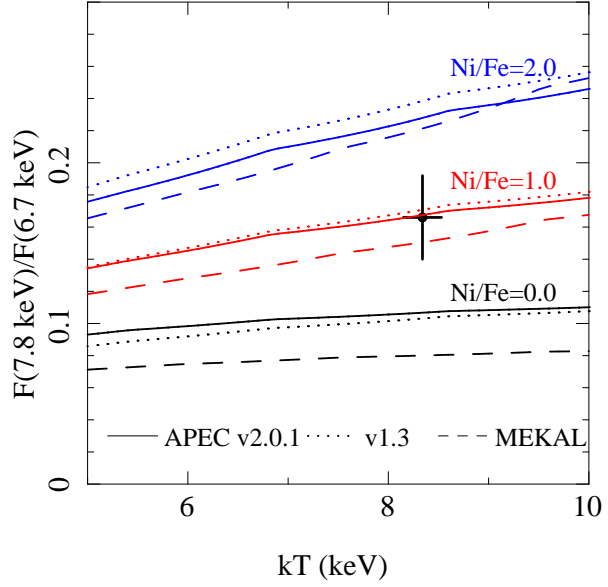


Fig. 5. The ratio of flux of the 7.8 keV line blend and $K\alpha$ line of He-like Fe, plotted against the plasma temperature. The observed line ratio of the central field of Suzaku is plotted as the solid closed circle with error bars. The solid, dotted, and dashed lines indicate theoretical line ratios according to APEC v2.0.1, APEC v1.3, and MEKAL plasma codes, respectively, with plasma of Ni/Fe ratio of 0, 1, and 2, in units of the solar ratio.

crepancy at the 8.3 keV line blend. The derived central energy of the Gaussian for the 8.3 keV blend, 8.27 ± 0.02 keV, is consistent with 8.26 keV of the mock spectra of the APEC models. However, it is significantly higher than the expected energy of 8.21 keV by the MEKAL model. The derived flux ratio of the 8.3 keV blend and the 6.7 keV line is consistent with the expectations by APEC and MEKAL codes. Therefore, the observed 8.3 keV line blend is more consistent with the APEC codes rather than the MEKAL code.

3.3. Iron-mass-to-light ratio

Because metals in the ICM have been synthesized in galaxies, the metal-mass-to-light ratio is a useful measure for studying the chemical evolution of clusters of galaxies. To estimate the integrated Fe mass profile, we fitted the annular spectra of MOS within an energy range of 1.6–5.0 keV with a APEC model to avoid uncertainties in the background. Here, the temperature and Fe abundance were restricted within error bars derived by Matsushita (2011). The derived emissivity profile is well fitted with a single β -model. The calculated density profile from the best-fit β -model agrees well within 10% with that by Briel et al. (1992) using ROSAT all sky survey data. We used the Fe abundance profile by Matsushita (2011) from XMM-Newton data and derived integrated mass profile of Fe in the ICM.

Because the K-band luminosity of a galaxy correlates well with the stellar mass, we calculated the luminosity profile of the K-band. We collected K-band magnitudes of galaxies in a 6×6 deg² box centered on the center of Coma

cluster from the Two Micron All Sky Survey (2MASS). We corrected foreground Galactic extinction of $A_K = 0.003$ (Schlegel et al. 1998) from the NASA/IPAC Extragalactic Database. The average surface brightness in the region at $100' < r < 170'$ was subtracted as the background. Then, we deprojected the brightness profile assuming a spherical symmetry and derived three-dimensional profile of K-band luminosity.

In addition, we calculated the luminosity profile of the B-band to compare previous papers and theoretical expectations. We collected B-band magnitude of member galaxies of the Coma cluster within $0.42 r_{180}$ by Michard & Andreon (2008) and within r_{180} by Doi et al. (1995). We corrected foreground Galactic extinction of $A_B = 0.036$ (Schlegel et al. 1998) from the NASA/IPAC Extragalactic Database. Then, we deprojected brightness profile as in the same manner as that for the K-band luminosity profile and derived a three-dimensional profile of B-band luminosity up to $0.5 r_{180}$. Since the data by Michard & Andreon (2008) is deeper than that by Doi et al. (1995), we scaled the brightness profile by Doi et al. (1995) to match that by Michard & Andreon (2008) and calculated the IMLR profile.

The derived IMLR profiles using K-band and B-band luminosity profiles are plotted in Figure 6. Here, the error bars include only the abundance errors. The cumulative profiles of the IMLR increase with radius up to $0.5 r_{180}$. At a given radius, the IMLR using B-band is a factor of 4–5 higher than that using the K-band. The difference in the normalizations between the two bands is consistent with a typical difference in the mass-to-light of stars in early-type galaxies (Nagino & Matsushita 2009). Therefore, the observed difference does not have a strong contribution from the different methods and data sets for the two bands.

4. Discussion

4.1. Contribution of SN Ia and SN II

The emission weighted average of the Si/Fe ratio of the ICM within $0.5 r_{180}$ of the Coma cluster from the line ratio is 0.99 ± 0.13 in solar units. This value is close to the ~ 0.8 in solar units of the Si/Fe ratios of the ICM of clusters and of groups with ICM temperatures smaller than several keV (Finoguenov et al. 2000; Rasmussen & Ponman 2007; Sato et al. 2007b; Sato et al. 2008; Sato et al. 2009b; de Grandi & Molendi 2009; Hayashi et al. 2009; Sato et al. 2011; Murakami et al. 2011; Sakuma et al. 2011) and early-type galaxies (Humphrey et al. 2006; Matsushita et al. 2007b; Tawara et al. 2008; Hayashi et al. 2009). This result indicates that the Si/Fe ratio of the ICM does not depend on the system mass because the Coma cluster is one of the largest clusters in the nearby universe.

Based on abundance ratios including Si and Fe, Finoguenov et al. (2000), Humphrey et al. (2006), de Plaa et al. (2007), Rasmussen & Ponman (2007), Sato et al. (2007b), and de Grandi & Molendi (2009) derived the contributions from SN Ia and SN II. They found that using

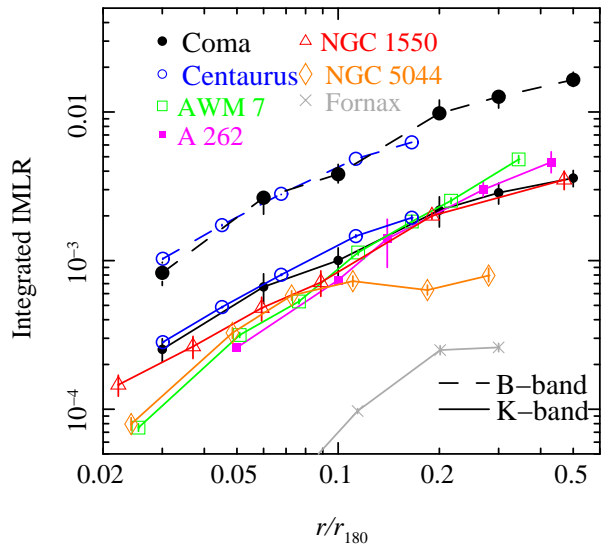


Fig. 6. Radial profiles of integrated IMLR in the K-band (solid lines) and B-band (dashed lines) of the Coma cluster (black filled circles), the Centaurus cluster ($kT = 3.9$ keV; blue open circles; Sakuma et al. 2011), AWM 7 cluster ($kT = 3.5$ keV; green open squares; Sato et al. 2008), Abell 262 cluster ($kT = 2.0$ keV; magenta filled squares; Sato et al. 2009b), NGC 1550 group ($kT = 1.2$ keV; red open triangles; Sato et al. 2010), NGC 5044 group ($kT = 1.0$ keV; orange diamonds; Komiyama et al. 2009), and the Fornax cluster ($kT = 1.3$ keV; gray; Murakami et al. 2011). Here, the difference in the solar abundance tables are considered.

a classical deflagration model, W7 (Iwamoto et al. 1999), for the theoretical SN Ia yield, over a half of Fe and a few tens % of Si in the ICM were synthesized in SN Ia. These papers also found that the contribution of SN Ia to Si strongly depends on the nucleosynthesis model: with a delayed detonation (DD) model, WDD1 (Iwamoto et al. 1999), about a half of Si comes from SN Ia.

We also calculated yield mixtures of nucleosynthesis models of SN II with metallicity = 0.02 by Nomoto et al. (2006) and SN Ia models of W7 and WDDs by Iwamoto et al. (1999). Using W7 and WDD3 models, to explain the observed Si/Fe ratio of 0.99 ± 0.13 in solar units, 60%–70% (20%–30%) of Fe (Si) were synthesized by SN Ia. Using the WDD1 model 70%–90% (40%–70%) of Fe (Si) were originated from SN Ia.

In contrast to Fe and Si, O and Mg are predominantly synthesized in SNe II. Abundance measurements covering a range of species from O to Fe are desired to constrain contributions and are therefore necessary to obtain unambiguous information on the history of formation of massive stars. Suzaku enabled us to measure O and Mg abundances in clusters and groups of galaxies with ICM temperatures smaller than several keV (Matsushita et al. 2007a; Sato et al. 2007a; Tokoi et al. 2008; Sato et al. 2008; ?; Komiyama et al. 2009; Sato et al. 2010; Sakuma et al. 2011; Murakami et al. 2011). The mixture of yields of W7 model and SN II gave better fits on the observed abundance pattern of O, Mg, Si, S and Fe in the ICM than that of WDD1 model and SN II (Sato et al. 2007a). With

the next Japanese X-ray satellite ASTRO-H, we will be able to detect the O line from the ICM around the X-ray peak of the Coma cluster.

4.2. Iron-mass-to-light ratio and constraints on initial mass function

Renzini (2005) calculated the ratios of the total amounts of O mass and Si mass synthesized by SN II to present stellar luminosity in a cluster. These ratios are very sensitive functions of the slope of the initial mass function (IMF): a decrease of the slope by 1 gives a factor of 20 higher O and Si masses at fixed present-day total stellar luminosity. Adopting a Salpeter IMF and O and Si yields by Woosley & Weaver (1995), the expected values (ICM and stars) of the oxygen-mass-to-light ratio (OMLR) and silicon-mass-to-light ratio (SMLR) are $\sim 0.1 M_{\odot}/L_{B,\odot}$ and $\sim 0.01 M_{\odot}/L_{B,\odot}$, respectively.

We compared the observed IMLR of the Coma cluster within $0.5 r_{180}$ with the expected values by Renzini (2005) for a entire cluster. At $0.5 r_{180}$, the integrated IMLR for the ICM using B-band luminosity is $0.016 \pm 0.001 M_{\odot}/L_{B,\odot}$. Adopting the Si/Fe ratio of 0.99 ± 0.13 in solar units, the integrated value of SMLR at $0.5 r_{180}$ is $0.009 \pm 0.001 M_{\odot}/L_{B,\odot}$. Adopting the W7 and WDD1 models for the SN Ia yield, the SMLR within this radius synthesized by SN II are $0.006\text{--}0.008 M_{\odot}/L_{B,\odot}$ and $0.002\text{--}0.005 M_{\odot}/L_{B,\odot}$, respectively. Assuming the solar stellar metallicity in cluster galaxies, the SMLR trapped in stars is $0.004 M_{\odot}/L_{B,\odot}$ for stellar mass-to-light ratio of 5 (Nagino & Matsushita 2009). As a result, the sum of SMLR in the stars and the ICM within $0.5 r_{180}$ is consistent with the expected SMLR of $\sim 0.01 M_{\odot}/L_{B,\odot}$, assuming a Salpeter IMF by Renzini (2005). The integrated IMLR profile of the Coma cluster increases with a radius up to $0.5 r_{180}$. If the MLRs continue to increase radially beyond $0.5 r_{180}$, a flatter, more top-heavy, IMF is necessary. Therefore, to study the slope of the IMF in clusters of galaxies, measurements of MLRs at outer regions of these systems are desired.

4.3. IMLR and dependence on the system mass

Figure 6 compares the integrated profile of IMLR of the Coma cluster with those of smaller systems observed with Suzaku, the AWM 7 cluster ($kT \sim 3.5$ keV; Sato et al. 2008), the Centaurus cluster ($kT \sim 3.9$ keV; Sakuma et al. 2011), Abell 262 cluster ($kT \sim 2.0$ keV; Sato et al. 2009b), the fossil group NGC 1550 ($kT \sim 1.2$ keV; Sato et al. 2010), the NGC 5044 group ($kT \sim 1.0$ keV; Komiyama et al. 2009), and the Fornax cluster ($kT \sim 1.3$ keV; Murakami et al. 2011) using Suzaku data. Here, differences in the solar abundance tables were corrected. The integrated IMLR of these clusters continues to increase with a radius within the observed regions, although the NGC 5044 group and the Fornax cluster show lower IMLR profiles, and become flatter at $0.2\text{--}0.3 r_{180}$. Within $0.1 r_{180}$, the derived IMLR profiles except the Fornax cluster agree with each other within a factor of two. At $0.2 r_{180}$, the integrated IMLR of the Coma clusters and poorer systems agree remarkably well, and beyond $0.2 r_{180}$, those of the Coma, Abell

262 clusters and the fossil group NGC 1550 system agree very well. At $0.35 r_{180}$, the AWM 7 cluster has a higher IMLR value than the Coma cluster. The similarity of the IMLR profiles and Si/Fe ratios among these clusters of galaxies indicates these systems have universal metal enrichment histories. The AWM 7 cluster was observed with Suzaku toward a direction to a filament of the large-scale structure, and the X-ray emission elongates with the same direction (Sato et al. 2008). The anisotropy may cause a discrepancy in the IMLR profile.

The dependence of the IMLR on the system mass confirms that derived from ASCA observations of groups and clusters of galaxies (Makishima et al. 2001) and also from Chandra observations (Rasmussen & Ponman 2009). Groups of galaxies differ from richer systems in that their IMLR are systematically smaller than those in rich clusters. Since the Fe abundances of systems plotted in Figure 6 at $0.1\text{--}0.5 r_{180}$ are consistent within error bars (?; Sato et al. 2010; Matsushita 2011), the difference in the IMLR reflects a difference in the ratio of gas and stellar mass. The stellar and gas mass fractions within r_{500} depend on the total system mass (Lin et al. 2003; Lin et al. 2004; Vikhlinin et al. 2006; Arnaud et al. 2007; Sun et al. 2009; Giardini et al. 2009). These studies found that the stellar-to-total-mass ratios within r_{500} of the groups are much larger than those in the clusters, whereas the gas mass fraction increases with the system mass. The observed higher stellar mass fraction and the lower gas mass fraction within r_{500} in poor systems, are occasionally interpreted as proof that the star formation efficiency depends on the system mass. However, as shown in Figure 6, the integrated IMLR–Fe abundance times gas mass per stellar mass– is a steep function of radius, which indicates that the gas is more extended than the stars in a cluster. The gas density profiles in the central regions of groups and poor clusters were observed to be shallower than those in the self-similar model, and the relative entropy level was correspondingly higher than that in rich clusters (Ponman et al. 1999; Ponman et al. 2003; Sun et al. 2009; Pratt et al. 2010). These deviations are considered to be best characterized by the injection of energy (pre-heating) into the gas before the clusters collapse (Kaiser 1991). Then, the difference in the ratio of gas mass to stellar mass may reflect differences in distributions of gas and stars, which reflects history of energy injection from galaxies to the ICM. To study the fractions of stars and gas in clusters of galaxies, measurements of gas and stellar mass beyond r_{500} are necessary.

4.4. Ni/Fe ratio

The observed flat Fe abundance of the Coma cluster within $0.2 r_{180}$ indicates that the gas has been mixed well. Since the Coma cluster does not have a strong cool core, the derived Ni/Fe ratio of the ICM is free from the resonant line scattering, and the effect of metals recently ejected by cD galaxies is small. In contrast, the cool core of clusters comprise a mixture of metals present in the ICM and supplied from the cD galaxy, which in turn contain metals that are synthesized by SN Ia and derived

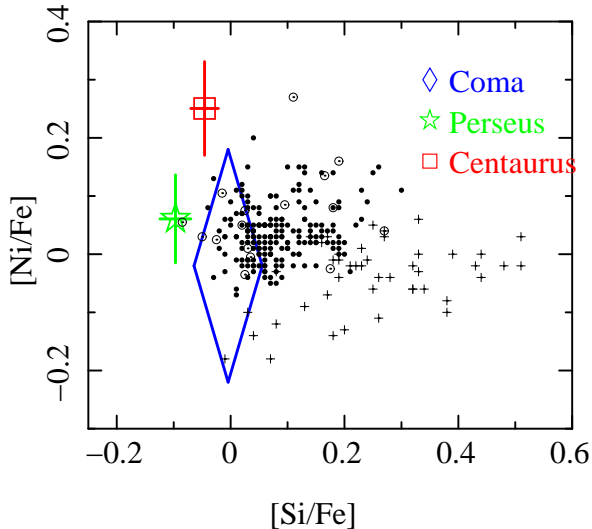


Fig. 7. $[\text{Ni}/\text{Fe}]$ of the central region of the Coma cluster (blue diamond), within ~ 50 kpc of the Perseus cluster (green star) and Centaurus cluster (red square) are plotted against $[\text{Si}/\text{Fe}]$. Values of the Galactic stars from Edvardsson et al. (1993), Feltzing & Gustafsson (1998), and Gratton et al. (2003) are also plotted as filled circles, open circles, and crosses, respectively.

from stars thorough stellar mass loss.

The observed Ni/Fe ratio in the Coma cluster is 0.6–1.5 solar, and is consistent with those observed in the cool cores derived by de Plaa et al. (2007). Figure 7 shows the observed abundance ratios of $[\text{Ni}/\text{Fe}]$ plotted against $[\text{Si}/\text{Fe}]$ for the central region ($<0.16 r_{180}$) of the Coma cluster and those in the cool cores of the Perseus and the Centaurus clusters (Matsushita & Tamura 2011). The figure also compares the abundance pattern with those of the Galactic stars. The stars with high $[\text{Si}/\text{Fe}]$ reflect the average Si/Fe ratio synthesized by SNe II in our Galaxy. The $[\text{Si}/\text{Fe}]$ of the three clusters are located around the stars with the smallest $[\text{Si}/\text{Fe}]$. The $[\text{Ni}/\text{Fe}]$ of the Coma cluster is consistent with those of the Galactic stars. Therefore, for the ICM in the Coma cluster, the abundance pattern of Si, Fe, and Ni is consistent with the same mixture of the yields of SN II and SN Ia in our Galaxy, and an additional source of metals is not required.

5. Conclusion

We analyzed XMM (up to $0.5 r_{180}$) and Suzaku (up to $0.16 r_{180}$) data of the Coma cluster, which is one of the largest clusters in the nearby Universe. Since the Coma cluster does not have a strong cool core and the Fe abundance in the ICM is flat up to $0.2 r_{180}$, the derived abundance pattern is not affected by recent metal supplies from the cD galaxies.

The Si/Fe ratios in the ICM are derived from the flux ratios of $\text{Ly}\alpha$ line of H-like Si and $\text{K}\alpha$ line of He-like Fe. The small temperature dependence of the line ratio limits the systematic uncertainty in the derived abundance

ratio. The derived Si/Fe ratio in the ICM shows no radial gradient. The emission weighted average of the Si/Fe ratio within $0.0\text{--}0.2 r_{180}$, $0.2\text{--}0.5 r_{180}$, and $0.0\text{--}0.5 r_{180}$ is 0.97 ± 0.11 , 1.05 ± 0.36 , and 0.99 ± 0.13 in units of solar ratio, using the solar abundance table by Lodders (2003). The comparison of the Si/Fe ratio of the Coma cluster with those of the smaller clusters indicates that dependence on the system mass of the Si/Fe ratio is small. The Ni/Fe ratio in the ICM is also derived from the flux ratio of the 7.8 keV line blend and $\text{K}\alpha$ line of He-like Fe. The derived Ni/Fe ratio is 0.6–1.5 solar. Therefore, the abundance pattern of Si, Fe, and Ni is consistent with the same mixture of the yields of SN II and SN Ia in our Galaxy.

We calculated the cumulative IMLR up to $0.5 r_{180}$ using K-band and B-band luminosities of galaxies. Considering the observed Si/Fe ratio, at $0.5 r_{180}$ the metal mass-to-light ratio in the ICM is consistent with expected value using a Salpeter IMF. However, if the IMLR continues to increase with a radius beyond $0.5 r_{180}$, a flatter IMF is necessary. The IMLR of the Coma cluster is similar to those of poor clusters with temperatures of 2–4 keV. These clusters may have universal metal enrichment histories.

References

- Anders, E., & Grevesse, N., 1989, *Geochim. Cosmochim. Acta*, 53, 197
- Arnaud, M., Aghanim, N., Gastaud, R., et al. 2001, *A&A*, 365, L67
- Arnaud, M., Pointecouteau, E., & Pratt, G. W. 2007, *A&A*, 474, L37
- Baumgartner, W. H., Loewenstein, M., Horner, D. J., & Mushotzky, R. F. 2005, *ApJ*, 620, 680
- Böhringer, H., Matsushita, K., Churazov, E., Finoguenov, A., & Ikebe, Y. 2004, *A&A*, 416, L21
- Briel, U. G., Henry, J. P. & Böhringer, H. 1992, *A&A*, 259, L31
- Churazov, E., Forman, W., Jones, C., Sunyaev, R., öhringer, H. 2004, *MNRAS*, 347, 29
- de Grandi, S., & Molendi, S. 2001, *ApJ*, 551, 153
- de Grandi, S., & Molendi, S. 2002, *Chemical Enrichment of Intracluster and Intergalactic Medium*, 253, 3
- de Grandi, S., & Molendi, S. 2009, *A&A*, 508, 565
- de Plaa, J., Werner, N., Bleeker, J. A. M., et al. 2007, *A&A*, 465, 345
- Doi, M., Fukugita, M., Okamura, S., & Tarusawa, K. 1995, *ApJS*, 97, 77
- Edvardsson, B., Andersen, J., Gustafsson, B., et al. 1993, *A&A*, 275, 101
- Evrard, A. E., Metzler, C. A., & Navarro, J. F. 1996, *ApJ*, 469, 494
- Feltzing, S., & Gustafsson, B. 1998, *A&AS*, 129, 237
- Finoguenov, A., David, L. P. & Ponman, T. J. 2000, *ApJ*, 544, 188
- Finoguenov, A., Arnaud, M. & David, L. P. 2001, *ApJ*, 555, 191
- Fukazawa, Y., Makishima, K., Tamura, T., Ezawa, H., Xu, H., Ikebe, Y., Kikuchi, K. & Ohashi, T. 1998, *PASJ*, 50, 187
- Fukazawa, Y., Makishima, K., Tamura, T., Nakazawa, K., Ezawa, H., Ikebe, Y., Kikuchi, K. & Ohashi, T. 2000, *MNRAS*, 313, 21

- Gratton, R. G., Carretta, E., Claudi, R., Lucatello, S., & Barbieri, M. 2003, *A&A*, 404, 187
- Giodini, S., et al. 2009, *ApJ*, 703, 982
- Hayashi, K., Fukazawa, Y., Tozuka, M., et al. 2009, *PASJ*, 61, 1185
- Humphrey, P. J., Buote, D. A., Gastaldello, F., et al. 2006, *ApJ*, 646, 899
- Iwamoto, K., Brachwitz, F., Nomoto, K., Kishimoto, N., Umeda, H., Hix, W. R., & Thielemann, F.-K. 1999, *ApJS*, 125, 439
- Johnson, R., Finoguenov, A., Ponman, T. J., Rasmussen, J., & Sanderson, A. J. R. 2011, *MNRAS*, 413, 2467
- Kaastra J.S. 1992, *An X-Ray Spectral Code for Optically Thin Plasmas* (Internal SRON-Leiden Report, updated version 2.0)
- Kaiser, N. 1991, *ApJ*, 383, 104
- Komiyama, M., Sato, K., Nagino, R., Ohashi, T., & Matsushita, K. 2009, *PASJ*, 61, S337
- Koyama, K., et al. 2007, *PASJ*, 59, 23
- Liedahl D. A., Osterheld A.L., & Goldstein W.H. 1995, *ApJ*, 438, L115
- Lin, Y.-T., Mohr, J. J., & Stanford, S. A. 2003, *ApJ*, 591, 749
- Lin, Y.-T., Mohr, J. J., & Stanford, S. A. 2004, *ApJ*, 610, 745
- Lodders, K. 2003, *ApJ*, 591, 1220
- Markevitch, M., Forman, W. R., Sarazin, C. L., & Vikhlinin, A. 1998, *ApJ*, 503, 77
- Makishima, K., et al. 2001, *PASJ*, 53, 401
- Matsushita, K., Finoguenov, A. & Böhringer, H. 2003, *A&A*, 401, 443
- Matsushita, K., et al. 2007a, *PASJ*, 59, 327
- Matsushita, K., Böhringer, H., Takahashi, I. & Ikebe, Y., 2007b, *A&A*, 462, 953
- Matsushita, K. 2011, *A&A*, 527, A134
- Matsushita, K. and Tamura, T., 2011, submitted to *A&A*
- Mewe R., Gronenschild E.H.B.M., & van den Oord G.H.J. 1985, *A&AS*, 62,197
- Mewe R., Lemen J.R., & van den Oord, G.H.J. 1986, *A&AS*, 65,511
- Michard, R., & Andreon, S. 2008, *A&A*, 490, 923
- Mitsuda, K., et al. 2007, *PASJ*, 59, 1
- Murakami, H., Komiyama, M., Matsushita, K., et al. 2011, *PASJ*, 63, 963
- Nagino, R., & Matsushita, K. 2009, *A&A*, 501, 157
- Nomoto, K., Tominaga, N., Umeda, H., Kobayashi, C., & Maeda, K. 2006, *Nuclear Physics A*, 777, 424
- Ponman, T. J., Cannon, D. B., & Navarro, J. F. 1999, *Nature*, 397, 135
- Ponman, T. J., Sanderson, A. J. R., & Finoguenov, A. 2003, *MNRAS*, 343, 331
- Pratt, G. W., et al. 2010, *A&A*, 511, A85
- Rasmussen, J., & Ponman, T. J. 2007, *MNRAS*, 380, 1554
- Rasmussen, J., & Ponman, T. J. 2009, *MNRAS*, 399, 239
- Renzini, A. 2005, *The Initial Mass Function 50 Years Later*, 327, 221
- Sakuma, E., Ota, N., Sato, K., Sato, T., & Matsushita, K. 2011, *PASJ*, 63, 979
- Sanders, J. S., & Fabian, A. C. 2006, *MNRAS*, 371, 1483
- Sato, K. et al. 2007a, *PASJ*, 59, 299
- Sato, K., Tokoi, K., Matsushita, K., Ishisaki, Y., Yamasaki, N. Y., Ishida, M. & Ohashi, T. 2007b, *ApJ*, 667, 41
- Sato, K., Matsushita, K., Ishisaki, Y., Yamasaki, N. Y., Ishida, M., Sasaki, S. & Ohashi, T. 2008, *PASJ*, 60, 333
- Sato, K., Matsushita, K., Ishisaki, Y., et al. 2009a, *PASJ*, 61, 353
- Sato, K., Matsushita, K. & Gastaldello, F., 2009b, *PASJ*, 61, 365
- Sato, K., Kawaharada, M., Nakazawa, K., Matsushita, K., Ishisaki, Y., Yamasaki, N. Y., & Ohashi, T. 2010, *PASJ*, 62, 1445
- Sato, T., Matsushita, K., Ota, N., et al. 2011, *PASJ*, 63, 991
- Schlegel, D. J., Finkbeiner, D. P., & Davis, M. 1998, *ApJ*, 500, 525
- Simionescu, A., Werner, N., Böhringer, H., et al. 2009, *A&A*, 493, 409
- Smith, R. K., Brickhouse, N. S., Liedahl, D. A., & Raymond, J. C. 2001, *ApJL*, 556, L91
- Sun, M., Voit, G. M., Donahue, M., Jones, C., Forman, W., & Vikhlinin, A. 2009, *ApJ*, 693, 1142
- Tamura, T., Kaastra, J. S., den Herder, J. W. A., Bleeker, J. A. M., & Peterson, J. R. 2004, *A&A*, 420, 135
- Tamura, T., Maeda, Y., Mitsuda, K., et al. 2009, *ApJL*, 705, L62
- Tawara, Y., Matsumoto, C., Tozuka, M., et al. 2008, *PASJ*, 60, 307
- Tokoi, K., et al. 2008, *PASJ*, 60, 317
- Vikhlinin, A., Forman, W., & Jones, C. 1994, *ApJ*, 435, 162
- Vikhlinin, A., Markevitch, M., Forman, W., & Jones, C. 2001, *ApJL*, 555, L87
- Vikhlinin, A., Kravtsov, A., Forman, W., Jones, C., Markevitch, M., Murray, S. S., & Van Speybroeck, L. 2006, *ApJ*, 640, 691
- Werner, N., de Plaa, J., Kaastra, J. S., et al. 2006, *A&A*, 449, 475
- Woosley, S. E., & Weaver, T. A. 1995, *ApJS*, 101, 181